

First-principles theory of resonant Raman intensity with application to MoS₂/WS₂ heterostructures

Yue Yu,¹ Jun Jiang,¹ Liangbo Liang,² Georgios D. Barmparis,³ Sokrates T. Pantelides,^{4,5} and X.-G. Zhang^{1,*}

¹*Department of Physics and the Quantum Theory Project,
University of Florida, Gainesville, Florida 32611, USA*

²*Center for Nanophase Materials Sciences, Oak Ridge National Laboratory, Oak Ridge, Tennessee 37831, USA*

³*Crete Center for Quantum Complexity and Nanotechnology,
Department of Physics, University of Crete, Heraklion 71003, Greece*

⁴*Department of Physics and Astronomy, Vanderbilt University, Nashville, TN 37235, USA*

⁵*Department of Electrical Engineering and Computer Science, Vanderbilt University, Nashville, TN 37235, USA*

(Dated: October 5, 2019)

Raman spectroscopy yields both peak positions and peak intensities. The latter contains greater amount of information but its utility is hampered by the lack of first-principles theory and accurate means of calculation for resonant Raman scattering. We present a such a theory for solids and show that it allows quantitative analysis of Raman intensity, potentially expanding the power of this experimental tool. Computationally challenging summations over all initial and final phonon configurations are carried out rigorously by a path-integration technique. The theory is demonstrated in an analysis of the experimental Raman spectrum of MoS₂/WS₂ heterostructures. The relative peak intensities are used to reveal the particular electronic states excited by the laser in each experiment, information hitherto unavailable to experimentalists.

Raman spectroscopy is an indispensable tool to characterize structural and electronic properties of 2D materials such as graphene, bilayer graphene, transition-metal dichalcogenides (2MDCs), and others.^{1–12} Resonant Raman signals, produced when the laser is tuned near the frequency of an electronic transition, are much stronger than nonresonant signals,¹³ making the former a more sensitive tool for probing low-dimensional materials. Examples include the discovery of new excitonic states in monolayer WS₂ and WSe₂,^{14,15} where the electron-phonon coupling is found to be different for the ground and excitonic states. Resonant Raman spectroscopy also provides the sensitivity to distinguish individual and few layers of WS₂¹⁶, and to identify the presence of defects with the extent of n-type or p-type doping¹⁷.

The theory of Raman spectroscopy under nonresonant conditions has been formulated in terms of perturbation theory in the framework of density functional theory (DFT).^{18,19} Under nonresonant conditions, one can invoke the Placzek approximation,²⁰ which assumes that the energy difference between the photon and the exciton is much greater than the phonon energies, allowing a simplification of the theory. However, serious complications arise when there is resonance. Resonant Raman signals show strong dependence on laser energy, power, and polarization, and possibly other uncontrolled factors (such as angle of incidence and duration) in experiments.^{9,21} Understanding such dependencies requires a quantitative theory, which is currently lacking for solids.

A formal theory established previously^{22–24} was applied to quantum-chemistry calculations of small molecules²⁵ or simple models for solids.²⁶ However, its general adoption was prevented by a conceptual difficulty that made most physicists to believe that this term should be zero for solids. The theoretical challenge is illustrated in Fig. 1, which represents the two-vertex process of resonant Raman scattering. For a coupled electron-phonon system, the electron-radiation interaction simultaneously causes the electronic state transition and the emission or absorption of phonons. Therefore, both interaction vertices intersect photon, phonon, and electron lines.

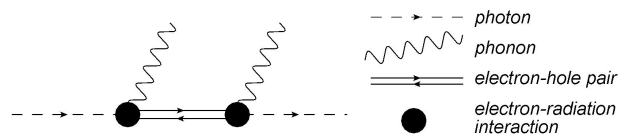


FIG. 1. Feynman diagram representation of resonant Raman scattering.

Such a term should vanish in a traditional interpretation of Feynman diagrams, which dictates that each interaction vertex corresponds to a perturbing Hamiltonian. If any phonons are absorbed or emitted at a vertex without an electron-phonon term in the Hamiltonian, the initial and final states should have different phonon numbers whereby their wave functions should be orthogonal, leading to a vanishing matrix element. Inclusion of an electron-phonon term requires one to insert additional vertices into the diagram, leading to a diagram of at least third order. Some of past resonant-Raman theories considered the diabatic terms as the main contribution, which are indeed higher-order.^{27,28} Such theories do not yield non-resonant theories under non-resonant conditions, casting doubts on their validity.

In this paper, we overcome this conceptual difficulty and show that the term represented by Fig. 1 does not vanish in a solid in a proper application of second-order perturbation theory, which leads to a result equivalent to the Franck-Condon principle²⁹. A first-principles method for resonant Raman spectroscopy of solids arising from this development is shown to be consistent with the previous formal theory. We also address the numerical challenge caused by the large number of phonon configurations, which is long-standing and common for all multi-phonon processes in molecules and solids. Methods including the Monte-Carlo method,³⁰ the semiclassical approximation,^{31,32} and conversion of the sum to a time correlation function³³ have been attempted but they require severe approximations or prohibitive computation resources. Our solution is a novel path-integral formulation. The power of the

method is demonstrated by first-principles calculations of the resonant Raman spectroscopy of MoS₂/WS₂ heterostructures. The calculated result is compared to experiments to reveal that the variation in experimental results arises from differences in the excited electronic states due to different laser energy and polarization. Different excited electronic states in turn contribute to vastly different intensities in Raman spectroscopy because of strong symmetry dependence of exciton-phonon coupling.

When one approximates the wave functions as the Born-Oppenheimer form, $|\Psi\rangle = |\psi_{\mathbf{R}}(\mathbf{r})\rangle|X(\mathbf{R})\rangle$, where $|\psi\rangle$ is the electron wave function and $|X\rangle$ is the phonon wave function, within the harmonic approximation for phonons, the parabolic potential energy surface (PES) for the phonon wave function $|X\rangle$ has the minimum at a location that depends on the electronic state due to the electron-phonon coupling. To see this, we write down a general form for the Hamiltonian of the electron-phonon system,

$$\hat{H}_{tot} = \hat{H}_e + \hat{H}_{ph} + \hat{H}_{e-ph}. \quad (1)$$

Within the harmonic approximation for phonons, the electron-phonon coupling is,

$$\hat{H}_{e-ph} = \sum_{n,j} g_{nj} \hat{c}_n^\dagger \hat{c}_n (\hat{a}_j^\dagger + \hat{a}_j) + \hbar \delta \omega_{nj} \hat{c}_n^\dagger \hat{c}_n \quad (2)$$

where n indicates the electronic states, j indicates the phonon modes, and $\delta \omega_{nj}$ is the change in the phonon frequency between the n th excited electronic state and the electronic ground state ($n = 0$). The minimum of the PES for mode j is at $-(g_{nj}/\omega_{nj}^2)\sqrt{2\omega_j/\hbar}$, where $\omega_j = \omega_{0j}$ is the phonon frequency of the electronic ground state (see Supplementary Information for detailed derivation).

Applying the second-order time-dependent perturbation theory, the Raman intensity due to the n th excited state is (see Supplementary Information for detailed derivation),

$$I_n(E_L) = \kappa' \sum_{i,a,f} \left| \frac{\langle X_f | X_a \rangle \langle X_a | X_i \rangle}{E_L - E_n - (\Theta_a - \Theta_i) + i\gamma_n} \right|^2 e^{-\beta\Theta_i} \times \delta[E_s + (\Theta_f - \Theta_i)] \quad (3)$$

where indices i, a, f label the initial, intermediate and final states, respectively. This is exactly the term depicted in Fig. 1, with the electronic part of the matrix elements absorbed into κ' . E_L is the incident laser energy, and E_n is the energy of n th excited state measured from the ground state energy. Θ are the phonon energies, and a parameter γ_n with unit of energy is introduced to represent the lifetime of the excited state. Electron-radiation interaction strength is included in κ' as a constant. The summations are over all possible phonon configurations. The initial states are assumed to be at thermal equilibrium and therefore are weighted by the Boltzmann factor $e^{-\beta\Theta_i}$ with $\beta = 1/k_B T$.

The matrix elements $\langle X_{i,f} | X_a \rangle$ result from the polarization-like phonon motion as described below. The phonon system initially moves along the PES of the ground electronic state. Under the radiation field, it jumps to the PES of the n th excited electronic state when the electronic

transition to the n th excited state occurs, then instantaneously jumps back to the PES of the ground electronic state but with a different (f) phonon configuration, simultaneously with the electronic system returning to the ground state by emitting a photon. The transitions occur without any nuclear motion, thus this describes exactly the same physical picture as the Franck-Condon principle²⁹. The matrix elements $\langle X_{i,f} | X_a \rangle$ when the phonon numbers are different are thus nonzero because $|X_{i,f}\rangle$ and $|X_a\rangle$ are on different PESes. In this regard, the resonant Raman signal is the result of phonon equilibrium positions changing between the electronic ground state and the intermediate excited state. Generally speaking, the greater the changes, the stronger the resonant Raman intensities.

The summation over all initial, final, and intermediate configurations presents the biggest numerical challenge in this theory. In order to make this approach feasible, we first reduce the summation into a more manageable form. We make use of the following,

$$\begin{aligned} & \frac{\langle X_f | X_a \rangle \langle X_a | X_i \rangle}{\Theta_i + E_L - \Theta_a - E_n + i\gamma} \\ &= -i \int_0^\infty dx \langle X_f | X_a \rangle \langle X_a | X_i \rangle e^{\frac{-\gamma+iE_L-iE_n}{\hbar}x} e^{\frac{i(\Theta_i-\Theta_a)}{\hbar}x} \\ &= -i \int_0^\infty dx \langle X_f | e^{-\frac{i\pi}{\hbar}\hat{H}_{ph}^n} | X_a \rangle \langle X_a | e^{\frac{i\pi}{\hbar}\hat{H}_{ph}^0} | X_i \rangle e^{\frac{-\gamma+iE_L-iE_n}{\hbar}x} \end{aligned} \quad (4)$$

where \hat{H}_{ph}^n are the phonon Hamiltonians of the n th PES. Next, we express the δ function in Eq. (3) as an integration over a time variable, in which the phonon part of the energies, Θ_i and Θ_f , are again converted to the operator \hat{H} .^{31,34} The full derivation is given in the supplementary material. The summation over the phonon configurations is carried out rigorously by contracting the repeated indices using the completeness relation. We finally obtain,

$$\begin{aligned} I_n(E_L) &= \kappa' \int_{-\infty}^\infty dt \int_0^\infty dx dy e^{-\frac{i}{\hbar}E_s t} e^{\frac{-\gamma+iE_L}{\hbar}x} e^{\frac{-\gamma-iE_L}{\hbar}y} \\ &\quad \times \text{Tr} \left[e^{\frac{i}{\hbar}\hat{H}_{ph}^n y} e^{\frac{i}{\hbar}\hat{H}_{ph}^0 t} e^{-\frac{i}{\hbar}\hat{H}_{ph}^n x} e^{-\frac{i}{\hbar}\hat{H}_{ph}^0(t-x+y)-\beta\hat{H}_{ph}^0} \right] \\ &= \kappa' \int_{-\infty}^\infty dt \int_0^\infty dx dy e^{-\frac{i}{\hbar}E_s t} e^{\frac{-\gamma+iE_L}{\hbar}x} e^{\frac{-\gamma-iE_L}{\hbar}y} \\ &\quad \times \prod_j \frac{e^{\frac{1}{2}(\Delta\omega_j x - \Delta\omega_j y + \beta\hbar\omega_j)}}{e^{(\Delta\omega_j x - \Delta\omega_j y + \beta\hbar\omega_j)} - 1} e^{iS_j F_j(x,y,t)} \end{aligned} \quad (5)$$

where the subscript j denotes the phonon modes, $\Delta\omega_j$ is the change in the phonon frequency between the excited electronic state and the ground electronic state, $S_j = \omega_j^2 \Delta q_j^2 / 2\hbar$ is a dimensionless measure of the change in the equilibrium position, Δq_j , for mode j .³⁵ $F_j(x, y, t)$ is a function whose explicit form is derived in the supplementary material. To arrive at the second equality, we projected the exponential operators onto bases formed by phonon wave functions expressed in the representation of the canonical coordinates,³⁴ turning the product and trace operations to integrations in the canonical coordinates domain. The matrix elements generated by

this projection are evaluated via the Feynman path-integral formula. The details of the derivation are given in the supplementary material.

We select MoS₂/WS₂ heterostructure to demonstrate the power of the first-principles method. A particularly interesting property of the optical absorption spectrum predicted for monolayer MoS₂ is the large and diverse number of bound excitonic states with different exciton energies and symmetries.^{36,37} Symmetry-dependent exciton-phonon coupling in monolayer, bilayer, and bulk MoS₂ has been studied using resonant Raman spectroscopy.^{38,39} Similar interesting optical and vibrational properties can be found in other TMDC family members such as WS₂, WSe₂, etc.^{16,40,41} Van der Waals heterostructures of different TMDCs often form type II electronic band alignments that can facilitate efficient electron-hole separation for light detection and harvesting.^{21,42} MoS₂/WS₂ heterostructures can also dissociate excitons effectively via charge separation which improves photon absorption.^{43,44}

A MoS₂/WS₂ heterostructure is a two-layered TMDC with van der Waals interaction between the layers. The relaxed structures of the electronic ground state and several excited states, and the phonon modes of these states, are calculated using Quantum Espresso.⁴⁵ The lattice mismatch between the two layers is small and we assume the MoS₂ lattice constant for the heterostructure. There are two types of stacking for a triangular lattice with two sublattices.¹² Our total energy calculation shows that the stacking with Mo on top of the S atom in the WS₂ layer (AB stacking) is lower in energy by 0.035 eV per unit cell than the stacking with Mo above the center of the triangle of the W sublattice (AA stacking). We will use the AB stacking in all subsequent calculations.

The electronic excited states are calculated using constrained DFT⁴⁶ in which the occupation numbers of the single electron states are fixed. In the case of MoS₂/WS₂ heterostructure, the ultrasoft pseudopotentials and the local density approximation (LDA) yield atomic structure and other properties in good agreement with experiment.⁴⁷ The electronic excited-state lattice relaxation is calculated using a supercell containing $5 \times 5 \times 1$ primitive cells (150 atoms) and $3 \times 3 \times 1$ k -points. The atoms on the supercell boundary are fixed to the ground-state positions. The relaxed structure is obtained with convergence criteria for the force less than 10^{-3} (atomic unit) and for the energy less than 10^{-4} Ryd. Vesta is used to visualize the spatial distribution of the charge density⁴⁸. We consider only first-order resonances, defined as scattering processes involving only phonons at the Γ point, where the crystal momentum is zero. With a sufficiently large supercell, the non- Γ point resonances are negligible. Phonopy⁴⁹ is used to generate frozen phonon configurations, using Quantum espresso as the force calculator. The force needed for the phonon modes of excited electronic states are calculated using constrained DFT.

In Fig. 2 we show the dependence of the intensity of the E_{2g_Mo} phonon peak at 389.9 cm^{-1} on the laser energy and the temperature. Because the resonance condition depends on the incoming laser energy, the intensity of the Raman peaks changes sensitively as a function of the laser energy

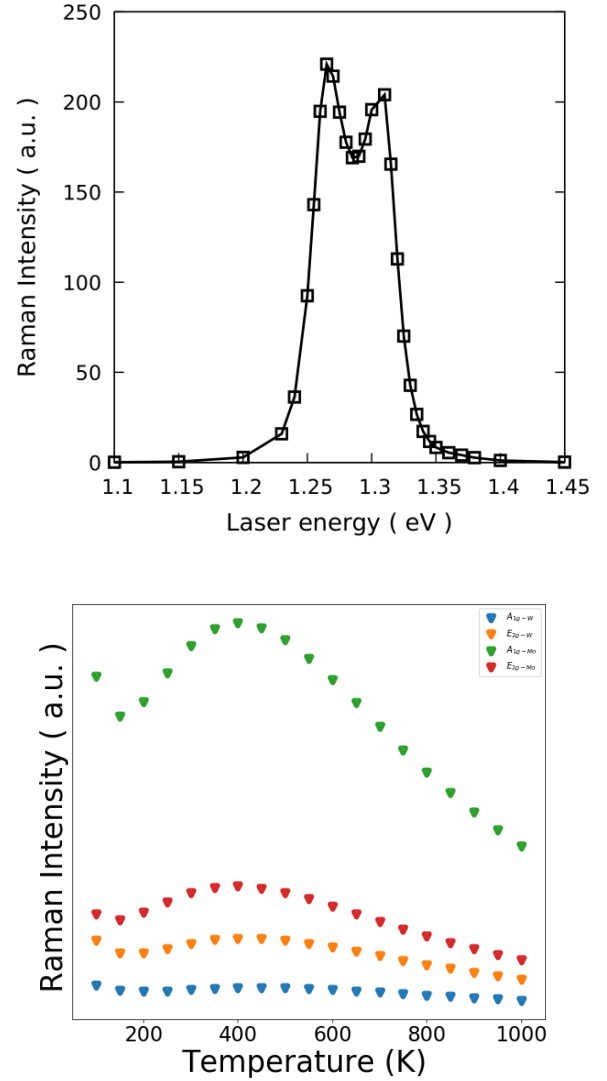


FIG. 2. Resonant Raman intensity of the E_{2g} mode of the Mo layer for $E_a = 1.5979 \text{ eV}$ as a function of the laser energy at $T = 300 \text{ K}$ (top panel) and as a function of the temperature with $E_L = 1.7 \text{ eV}$ (bottom panel). Both calculations are done with $\gamma = 15 \text{ meV}$.

E_L . The calculation is performed with the excited electronic state at $E_a = 1.5979 \text{ eV}$ and the smearing parameter $\gamma = 15 \text{ meV}$. The value of smearing is chosen to ensure fast convergence of the calculation. It is several times larger than actual smearing fitted from experiments (see below). There are two resonances, one at $E_L = E_a$, when the phonon emission occurs during the emission of the photon, and the other at $E_L = E_a + \Theta_a - \Theta_i$, when the phonon emission occurs during the absorption of the photon.

The present theory naturally yields a temperature dependence of Raman intensity. The calculation is performed for the excited electronic state at $E_a = 1.5979 \text{ eV}$, and laser energy $E_L = 1.7 \text{ eV}$. We assume that the exciton smearing arises from electron-phonon coupling and thus is a linear function of temperature, $\gamma = CT$, and require that $\gamma = 15 \text{ meV}$ at $T = 300 \text{ K}$. At low temperatures, Raman intensity increases

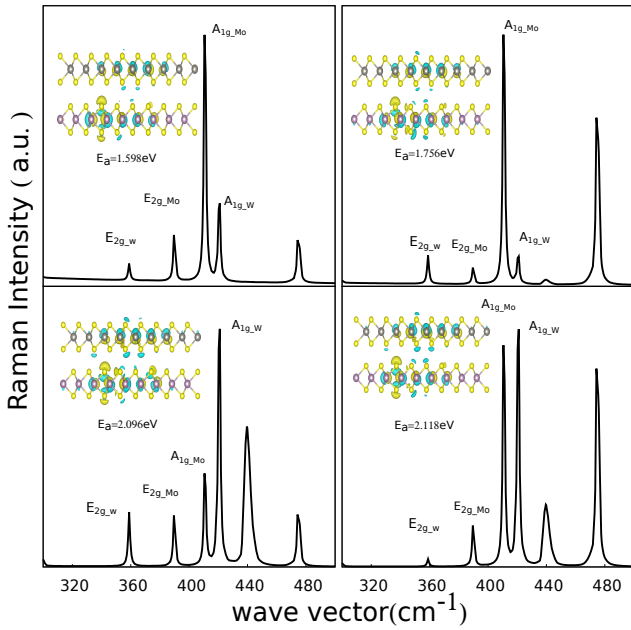


FIG. 3. Calculated resonant Raman spectra for individual excited electronic states in MoS₂/WS₂ heterostructure. Insets show the corresponding excited state charge density distribution.

with temperature, since the phonon occupation number grows rapidly. At high temperatures, the intensity drops due to stronger electron-phonon coupling that leads to an increased γ in the numerator of Eq. (3) and overwhelms the slower increase in the denominator. Such a trend is in agreement with measurements of single layer WS₂ Raman spectra⁵⁰, where the intensity of both Raman peaks first increases rapidly with temperature from 83 K to 200 K then decreases gradually at higher temperatures.

In Fig. 3 we show calculated resonant Raman intensities for four excited electronic states and, in the insets, the charge density distribution for each state. In these calculations, we set $E_L = 2.3305$ eV (532 nm), and $\gamma = 15$ meV. As an example of the symmetry dependent exciton-phonon coupling, note the dramatic difference in the relative intensity ratios of the two A_{1g} peaks. For the $E_a = 1.598$ eV and $E_a = 1.756$ eV states, the A_{1g_W} peak is much lower than the A_{1g_Mo} peak, but for the $E_a = 2.096$ eV and $E_a = 2.118$ eV states, the opposite is seen. To explain this feature, we note that charge transfer between the two layers in each excited electronic state causes the equilibrium positions of the layers to be displaced. Such displacements are projected into the phonon normal mode displacements as Δq_j , which in turn through S_j in Eq. (5) leads to phonon mode signatures in the resonant Raman intensity. Because the charge transfer is localized, the local displacements of the atoms can be quite significant, up to 0.01 Å for the S atoms for all four excited electronic states. However, the magnitude of the displacements of the individual S atoms does not correlate with the ratio of the A_{1g} peaks. This result is caused by the fact that each excited electronic state breaks

the lattice symmetry differently. When the displacements of all S atoms within the same layer are averaged, the average value correlates strongly with the A_{1g} peak ratios. Both the largest displacements and the average values are listed in the Supplementary Material. The relative intensity of the resonant Raman peaks is thus explained by the symmetric components of the atomic displacements of each electronic excited state projected onto the phonon modes.

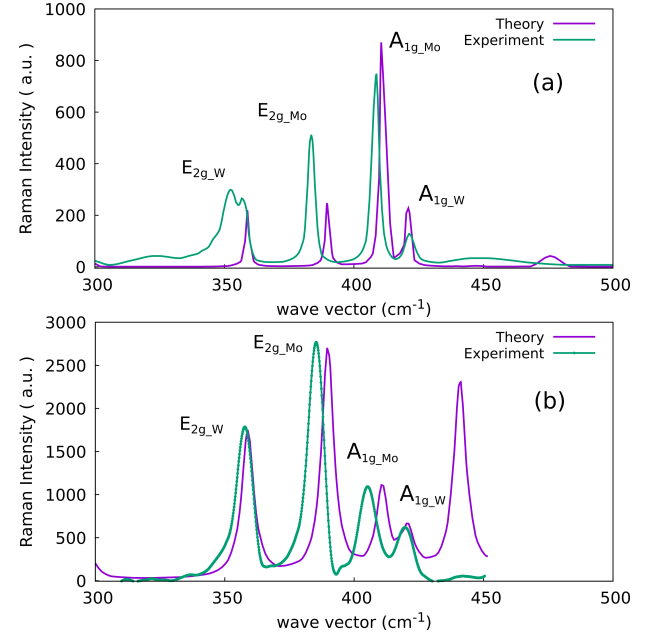


FIG. 4. Calculated resonant Raman intensities (purple) compared to experimental data (green).

An important conclusion from the above analysis is that comparing the calculated resonant Raman spectrum with an experimental measurement enables one to identify the electronic excited state(s) being measured by the particular experiment. We demonstrate this in Fig. 4, which shows the comparison of the calculated resonant Raman intensity with two sets of experimental data.^{9,21} For the first set,⁹ shown in Fig. 4a, we identify the electronic excited state to be the one at $E_a = 1.5979$ eV. The best fit is obtained with $\gamma = 3.2$ meV, and $E_L = 1.641$ eV. This energy is substantially lower than the experimental incident laser energy of 2.3305 eV (532 nm), needed to cancel the DFT error that typically underestimates the excited electronic state energy and ensure the resonance condition.

The second set of experimental data²¹ (Fig. 4b) is found to be consistent with a mixture of $E_a = 2.0066$ eV and $E_a = 2.0369$ eV electronic excited states. In this case the best fit is with $\gamma = 4$ meV and $E_L = 2.039$ eV. This energy is lower than the experimental laser energy of 2.54066 eV (488 nm) by a similar amount as in the case of the first experiment. For this data set, the theory shows an extra peak at 440 cm⁻¹ that is absent in the experimental spectrum. This peak corresponds to an out-of-plane phonon mode in the W layer (see the table in supplementary material). In this mode the W atom and the two S atoms move in opposite directions, producing

an oscillating dipole moment along the z direction. Such motions may be quenched in the presence of a substrate, whose dielectric response tends to counteract these motions. In contrast, the A_{1g} mode induces minimal dipole moment change, whereby it is less likely to be suppressed by the substrate response.

In summary, we have reformulated the theory of resonant Raman spectroscopy for periodic solids, taking multi-phonon processes into full account. This theory is applied to MoS₂/WS₂ heterostructures, and yields different Raman peaks and intensities as a function of electronic excited-state energies, laser energy, and temperature. The coupling between the electronic excited states and the phonon normal modes is shown to arise from the changes in the equilibrium atomic positions due to electronic excitation. Quantitative comparison between calculation and experiment enables the identification of the particular electronic excited state(s) participating in the resonant Raman process. This feature of the

theory can greatly enhance the power of Raman spectroscopy in understanding intricate electron (exciton)-phonon coupling in 2D materials and their heterostructures.

ACKNOWLEDGMENTS

This work was supported by NSF grant 1508898. GDB was supported by the EU/FP7-REGPOT-2012-2013-1 under grant agreement no. 316165. A portion of this research was conducted at the Center for Nanophase Materials Sciences, which is a DOE Office of Science User Facility. The authors acknowledge University of Florida Research Computing for providing computational resources and support that have contributed to the research results reported in this publication. URL: <http://researchcomputing.ufl.edu> This work used the Extreme Science and Engineering Discovery Environment (XSEDE), which is supported by National Science Foundation grant number ACI-1548562.

* Email: xgz@ufl.edu

- ¹ B. Radisavljevic, A. Radenovic, J. Brivio, i. V. Giacometti, and A. Kis, Nat. Nanotechnol. **6**, 147 (2011).
- ² A. Splendiani, L. Sun, Y. Zhang, T. Li, J. Kim, C.-Y. Chim, G. Galli, and F. Wang, Nano Lett. **10**, 1271 (2010).
- ³ K. F. Mak, C. Lee, J. Hone, J. Shan, and T. F. Heinz, Phys. Rev. Lett. **105**, 136805 (2010).
- ⁴ Q. H. Wang, K. Kalantar-Zadeh, A. Kis, J. N. Coleman, and M. S. Strano, Nat. Nanotechnol. **7**, 699 (2012).
- ⁵ D. Jariwala, V. K. Sangwan, L. J. Lauhon, T. J. Marks, and M. C. Hersam, ACS nano **8**, 1102 (2014).
- ⁶ N. Zibouche, P. Philipsen, A. Kuc, and T. Heine, Phys. Rev. B **90**, 125440 (2014).
- ⁷ V. Podzorov, M. E. Gershenson, C. Kloc, R. Zeis, and E. Bucher, Appl. Phys. Lett. **84**, 3301 (2004).
- ⁸ L. Liu, S. B. Kumar, Y. Ouyang, and J. Guo, IEEE Trans. Electron Devices **58**, 3042 (2011).
- ⁹ N. Huo, J. Kang, Z. Wei, S.-S. Li, J. Li, and S.-H. Wei, Adv. Funct. Mater. **24**, 7025 (2014).
- ¹⁰ C. Lee, H. Yan, L. E. Brus, T. F. Heinz, J. Hone, and S. Ryu, ACS Nano **4**, 2695 (2010).
- ¹¹ A. A. Puretzky, L. Liang, X. Li, K. Xiao, K. Wang, M. Mahjouri-Samani, L. Basile, J. C. Idrobo, B. G. Sumpter, V. Meunier, and D. B. Geohegan, ACS nano **9**, 6333 (2015).
- ¹² J. Zhang, J. Wang, P. Chen, Y. Sun, S. Wu, Z. Jia, X. Lu, H. Yu, W. Chen, J. Zhu, G. Xie, R. Yang, D. Shi, X. Xu, J. Xiang, K. Liu, and G. Zhang, Adv. Mater. **28**, 1950 (2016).
- ¹³ E. Smith and G. Dent, *Modern Raman Spectroscopy* (John Wiley & Sons, Inc., Hoboken, 2005).
- ¹⁴ E. del Corro, H. Terrones, A. Elias, C. Fantini, S. Feng, M. A. Nguyen, T. E. Mallouk, M. Terrones, and M. A. Pimenta, ACS Nano **8**, 9629 (2014).
- ¹⁵ E. del Corro, A. Botello-Méndez, Y. Gillet, A. L. Elias, H. Terrones, S. Feng, C. Fantini, D. Rhodes, N. Pradhan, L. Balicas, X. Gonze, J.-C. Charlier, M. Terrones, and M. A. Pimenta, Nano Lett. **16**, 2363 (2016).
- ¹⁶ A. Berkdemir, H. R. Gutiérrez, A. R. Botello-Méndez, N. Pereira-López, A. L. Elías, C.-I. Chia, B. Wang, V. H. Crespi, F. López-Uriás, J.-C. Charlier, H. Terrones, and M. Terrones, Sci. Rep. **3**, 1755 (2013).
- ¹⁷ J. P. Bonacum, A. O'Hara, D.-L. Bao, O. S. Ovchinnikov, Y.-F. Zhang, G. Gordeev, S. Arora, S. Reich, J.-C. Idrobo, R. F. Haglund, S. T. Pantelides, and K. I. Bolotin, Phys. Rev. Materials **3**, 064004 (2019).
- ¹⁸ M. Lazzeri and F. Mauri, Phys. Rev. Lett. **90**, 036401 (2003).
- ¹⁹ Y. Gillet, M. Giantomassi, and X. Gonze, Phys. Rev. B **88**, 094305 (2013).
- ²⁰ B. Peter, *Phonons: Theory and Experiments II* (Springer-Verlag Berlin Heidelberg, 1986).
- ²¹ X. Hong, J. Kim, S.-F. Shi, Y. Zhang, C. Jin, Y. Sun, S. Tongay, J. Wu, Y. Zhang, and F. Wang, Nat. Nanotechnol. **9**, 682 (2014).
- ²² R. Loudon, J. Phys. **26**, 677 (1965).
- ²³ H. A. Kramers and W. Heisenberg, Z. Angew. Phys. **31**, 681 (1925).
- ²⁴ M. Cardona, Top. Appl. Phys. **50**, 107 (1982).
- ²⁵ E. J. H. See-Y. Lee, J. Chem. Phys. **71**, 4777 (1979).
- ²⁶ V. Perebeinos and P. B. Allen, Phys. Rev. B **64**, 085118 (2001).
- ²⁷ P. Y. Yu and M. Cardona, *Fundamentals of Semiconductors* (Springer, 2010) p. 383.
- ²⁸ B. R. Carvalho, L. M. Malard, J. M. Alves, C. Fantini, and M. A. Pimenta, Phys. Rev. Lett. **114**, 136403 (2015).
- ²⁹ M. Lax, J. Chem. Phys. **20**, 1752 (1952).
- ³⁰ G. D. Barmparis, Y. S. Puzyrev, X.-G. Zhang, and S. T. Pantelides, Phys. Rev. B **92**, 214111 (2015).
- ³¹ E. J. Heller, J. Chem. Phys. **68**, 677 (1978).
- ³² E. J. Heller, Acc. Chem. Res. **14**, 368 (1981).
- ³³ F. J. A. Ferrer, J. Cerezo, J. Soto, R. Improta, and F. Santoro, Comput. Theor. Chem. **1040-1041**, 328 (2014).
- ³⁴ L. Shi, K. Xu, and L.-W. Wang, Phys. Rev. B **91**, 205315 (2015).
- ³⁵ H. Kun and A. Rhys, Proc. R. Soc. London, Ser. A **204**, 406 (1950).
- ³⁶ D. Y. Qiu, F. H. da Jornada, and S. G. Louie, Phys. Rev. Lett. **111**, 216805 (2013).
- ³⁷ D. Y. Qiu, F. H. da Jornada, and S. G. Louie, Phys. Rev. Lett. **115**, 119901 (2015).
- ³⁸ B. R. Carvalho, L. M. Malard, J. M. Alves, C. Fantini, and M. A.

- Pimenta, Phys. Rev. Lett. **114**, 136403 (2015).
- ³⁹ B. R. Carvalho, L. M. Malard, J. M. Alves, C. Fantini, and M. A. Pimenta, Phys. Rev. Lett. **116**, 089904 (2016).
- ⁴⁰ H. Terrones, E. Del Corro, S. Feng, J. Poumirol, D. Rhodes, D. Smirnov, N. Pradhan, Z. Lin, M. Nguyen, A. Elías, T. E. Mal-louk, L. Balicas, M. A. Pimenta, and M. Terrones, Sci. Rep. **4**, 4215 (2014).
- ⁴¹ K. He, N. Kumar, L. Zhao, Z. Wang, K. F. Mak, H. Zhao, and J. Shan, Phys. Rev. Lett. **113**, 026803 (2014).
- ⁴² C.-H. Lee, G.-H. Lee, A. M. van der Zande, W. Chen, Y. Li, M. Han, X. Cui, G. Arefe, C. Nuckolls, T. F. Heinz, J. Guo, J. Hone, and P. Kim, Nat. Nanotechnol. **9**, 676 (2014).
- ⁴³ Y. Yu, S. Hu, L. Su, L. Huang, Y. Liu, Z. Jin, A. A. Purezky, D. B. Geohegan, K. W. Kim, Y. Zhang, and L. Cao, Nano Lett. **15**, 486 (2015).
- ⁴⁴ H. Wang, J. Bang, Y. Sun, L. Liang, D. West, V. Meunier, and S. Zhang, Nat. Commun. **7**, 11504 (2016).
- ⁴⁵ P. Giannozzi *et al.*, J. Phys.: Condens. Matter **21**, 395502 (2009).
- ⁴⁶ B. Kaduk, T. Kowalczyk, and T. Van Voorhis, Chem. Rev. **112**, 321 (2012).
- ⁴⁷ L. Liang and V. Meunier, Nanoscale **6**, 5394 (2014).
- ⁴⁸ K. Momma and F. Izumi, J. Appl. Crystallogr. **44**, 1272 (2011).
- ⁴⁹ L. Chaput, A. Togo, I. Tanaka, and G. Hug, Phys. Rev. B **84**, 094302 (2011).
- ⁵⁰ X. Huang, X. Huang, T. Yang, W. Ren, H.-M. Cheng, and T. Lai, Sci. Rep. **6**, 32236 (2016).